Chemical Engineering Journal 519 (2025) 165231

Contents lists available at ScienceDirect

Chemical Engineering Journal

journal homepage: www.elsevier.com/locate/cej

Electron “push-push-pull” type dithienopyrrole-based self-assembled monolayers on NiOx for enhanced performance of tin perovskite solar cells

Rajendiran Balasaravanan [a,1], Chun-Hsiao Kuan [b,1], Yun-Sheng Shih [b,1], Hsu-Lung Cheng [b], Deebakkrishnan Ganesan [a], Shao-Huan Hong [c], Cheng-Liang Liu [c], Yun-Rou Zhong [a], Xianyuan Jiang [e], Ming-Chou Chen [a,*], Eric Wei-Guang Diau [b,d,**]

[a] *Department of Chemistry, National Central University, Taoyuan 32001, Taiwan*
[b] *Department of Applied Chemistry and Institute of Molecular Science, National Yang Ming Chiao Tung University, Hsinchu 300093, Taiwan*
[c] *Department of Materials Science and Engineering, National Taiwan University, Taiwan*
[d] *Center for Emergent Functional Matter Science, National Yang Ming Chiao Tung University, Hsinchu 300093, Taiwan*
[e] *School of Physical Science and Technology, ShanghaiTech University, Shanghai 201210, China*

ARTICLE INFO

Keywords:
Dithienopyrrole
Tin perovskite solar cells
Nickel oxide (NiOx)
Phosphonic acid
Power conversion efficiency

ABSTRACT

A series of donor-donor-acceptor (D-D-A) type of dithienopyrrole (DTP) based self-assembled monolayer molecules (SAMs) were developed for modulation of NiOx and served as hole transporting materials (HTMs) for tin-based perovskite solar cells (TPSCs). The electron-donating DTP cores with various alkyl chains were asymmetrically functionalized with triphenylamine (TPA) electron donor at one side and conjugatedly end-capped with cyanophosphonic acid (**PA**) or cyanoacetic acid (**CA**) as an anchoring group to interact with NiOx. The two electron-donating (ED) units, TPA and DTP, are conjugated in a linear structure using an ED push-push design strategy to facilitate efficient charge transfer. The single crystal structures of **DTP-PE** (**1-OMe**) and **DTP-CA (3)** were obtained and revealed the planar nature of the dithienopyrrole core relative to the anchoring group, which facilitated easy SAM molecular alignment and stacking, thereby promoted the formation of a uniform SAM on the NiOx surface. For the perovskite layer preparation using a traditional one-step fabrication method, a rapid nucleation between SnI_2 and FAI occurred. Nevertheless, via a successful two-step spin coating technique, the DTP-scaffold SAMs/NiOx hybrid interfacial layer in TPSCs exhibited improved perovskite layer crystallization, leading to enhanced efficiency and stability. Among the new SAMs exploration, the electron push-push-pull type **DTP-PA (1)** based TPSCs exhibited the highest hole mobility and the slowest charge recombination, resulting in a high power conversion efficiency of 8.7% with great shelf-storage stability, retaining approximately 90% of its initial values after 3600 h of shelf storage. This study aims to address these issues for replacing commonly used hygroscopic PEDOT:PSS by incorporating new hydrophobic DTP-based SAMs on the cost effective NiOx hole transport layer/Sn-perovskite interface, marking the highest reported efficiency for organic dye-based SAM/NiOx as HTM in TPSCs.

1. Introduction

The emergence of hybrid perovskites in optoelectronic devices has aroused great research interest in recent decades due to their exceptional light harvesting ability, higher carrier mobility, good processability in solution and long carrier diffusion lengths [1–4]. In the recent literature, perovskite solar cells (PSCs) have shown remarkable efficiency improvement, soaring from an initial efficiency of 3.8% to over 26.7% [5–10]. However, the presence of toxic lead in PSCs is still a critical concern [11–13]. To address this point, tin-based perovskite solar cells (TPSCs) as a promising lead-free PSCs alternative have been explored and currently attaining a notable PCE of 16.05% [14–16].

---

[*] Corresponding author.
[**] Correspondence to: E. W-G. Diau, Department of Applied Chemistry and Institute of Molecular Science, National Yang Ming Chiao Tung University, Hsinchu 300093, Taiwan.
E-mail addresses: mcchen@ncu.edu.tw (M.-C. Chen), diau@nycu.edu.tw (E.W.-G. Diau).
[1] Rajendiran Balasaravanan, Chun-Hsiao Kuan and Yun-Sheng Shih contributed equally to this work.

https://doi.org/10.1016/j.cej.2025.165231
Received 7 April 2025; Received in revised form 20 June 2025; Accepted 22 June 2025
Available online 23 June 2025
1385-8947/© 2025 Elsevier B.V. All rights are reserved, including those for text and data mining, AI training, and similar technologies.

Although TPSC performance currently lags behind its lead-based analogue, tin perovskites possess a smaller bandgap and high charge carrier mobilities, which theoretically indicate that TPSC should have a higher maximum achievable PCE compared to lead-based PSC [15,17,18]. Various additive engineering strategies have been employed to address challenges such as the oxidation of Sn^{2+}/Sn^{4+} suppression [19], the surface defect passivation (self-doping) [20], and the crystal growth regulation in TPSCs [21], leading to enhanced efficiency and stability.

The use of charge-selective contact layers has been a key to attain high efficiency for a PSC device. However, the long-term stability of halide perovskites remains an obstacle to widespread industrial adoption [22,23]. In order to improve device stability, it's important to increase the basic stability of both halide perovskites and contact layers [24,25]. Many hole transporting materials (HTMs) are widely explored to enhance the performance of a PSC device [26]. Notably, inorganic NiOx exhibits good hole transport capabilities and greater stability compared to many organic HTL materials [27]. According to existing literature, some of the high-performance lead PSCs have utilized NiOx as the HTM and achieved PCE higher than 20% [28]. However, the potential use of NiOx in achieving high-performance TPSCs has rarely been explored. Despite its advantages as an HTL, the performance of NiOx is still hindered by defects at the interface with perovskite [29,30].

The challenges posed by expensive organic materials as sole hole transporting materials have driven researchers to explore alternative options, including new organic conjugated materials like self-assembled monolayers (SAMs). SAMs, such as **MPA-BT-CA** used in lead based PSCs have demonstrated a PCE of 21.24% [31], marking the first instance of a simple SAM achieving a PCE exceeding 20%. More recently the use of SAMs has led to a record breaking PCE of over 26.3% in PSCs [32]. In contrast to expensive and unstable organic hole-selective materials, SAMs offer cost-effective materials, that are scalable, stable, and easy to process without the need for dopants [27]. They also modify the work function of metal oxide surfaces, improving the alignment of energy bands in solar cells [33]. This variation is achieved by SAM anchoring groups, such as electron-withdrawing cyanocarboxylic acid (**CA**) [34] or cyanophosphonic acid (**PA**) [35], which have a chemical affinity for metal oxide hydroxyl groups, leading to dissociative chemisorption with the OH bond breaking. These functional and anchoring groups serve to optimize interface and surface properties, improve functionalities, charge extraction, wetting characteristics and are key to defining packing geometries [36]. The packing geometries are governed by the linkage group located between the anchoring and functional groups. As a result, several small molecular HTMs based on SAMs have been created and demonstrated high PCEs in both Pb-based and Sn-based PSCs. For instance, as depicted in Fig. 1a, **Me4PACZ** [37] and **LS-2** [38] (a non-conjugated SAM) featuring a phosphonic acid anchoring group, achieved an impressive efficiency of 24.5% in Pb-based PSCs. Similarly, conjugated organic small molecules that include phosphonic acid anchoring groups have shown excellent performance. For example, **4PA-Spiro** [39], **PTZ-CPA** [40], **GM-4PACz** [41], and **Ph-4PACz** [42], achieved very high efficiencies of 25.28%, 25.35%, 25.52%, and 25.60%, respectively. Very recently, by employing an electron donor (ED) push-push design strategy, with an acetyl-functionalized TPA topped on the carbazolyl core, **DTBA-2PACz** achieved a remarkable PCE up to 26.3% developed by Liu et al. [32].

For the SAMs developed for TPSCs, D.-W. Kang's group developed a MeO-2PACz SAM and incorporated it at the PEDOT:PSS HTL interface, achieving an impressive PCE of 12.16% [43]. Similarly, Yu et al. blended MeO-2PACz with 6-phosphonohexanoic acid (6PA) to engineer a compatible tin-perovskite thin film, resulting in a PCE of 9.4% [44]. Additionally, (4-(7H-dibenzo[*c*,*g*]carbazol-7-yl)ethyl)phosphonic acid (2PADBC) into the perovskite–NiOx interface effectively suppressed Sn^{2+} oxidation and passivated defects, achieving a high PCE of 14.19% for the small-area device and 12.05% for the large-area (1 cm^2) device and maintaining over 93% of the initial efficiency after 1000 h [45]. Our team recently designed a thienopyrazine-based SAM (**TP-MN**; as shown in Fig. 1b) and applied it to a NiOx film as a HTM, achieving a notable PCE of 7.7% [46]. More recently, PA-anchored **PTzBr-PA** [47] and the Y-shaped TPA-based **TPAT-CA** [48] were developed and achieved PCEs of 7.8% and 8.1%, respectively. In particular, with the unusual di-anchoring design, the X-shaped di-CA-anchored quinoxaline-based SAM **TQxD** achieved a PCE of 8.3% in TPSCs [49]. Based on these findings, this study develops a new series of D-D-A type SAM molecules to explore the enhanced performance for TPSCs, as depicted in Fig. 1c.

As shown in Fig. 1a, the TPA-based SAM, such as **LS-2**, had achieved an excellent PCE up to 24.5% [38], demonstrating an outstanding charge-selective ability of this simple unit. Carbazole-based SAMs, such as **GM-4PACz** [42] and **Ph-4PACz** [43], recently accomplished extraordinary PCE >25.5%, showing a superior charge-selective/directive ability of this more planar electron donative unit. Furthermore, by employing an ED push-push design strategy on the TPA-

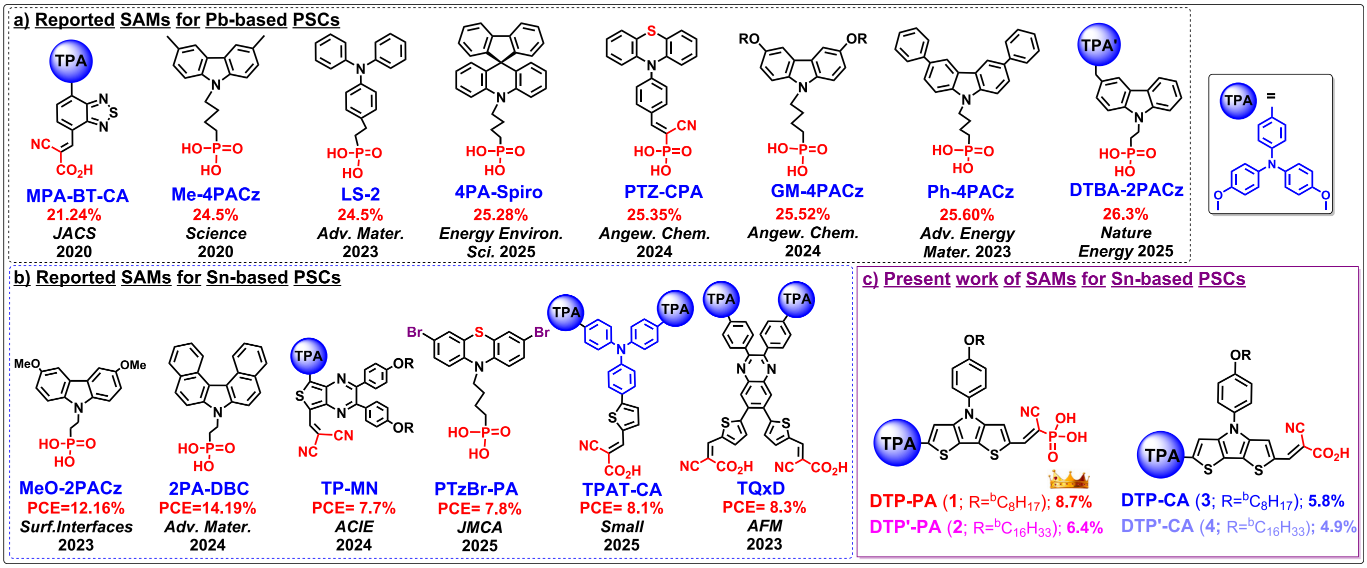

Fig. 1. Illustration of the structural formulas of self-assembled monolayers (SAMs) reported for (a) Pb-based PSCs, (b) Sn-based PSCs (TPSCs), and (c) chemical structures of dithienopyrrole-based SAMs for TPSCs studied in this work.

carbazole core, the new SAM **DTBA-2PACz** has achieved a record-breaking efficiency of 26.3% [33]. Building upon the similar ED push-push concept as **DTBA-2PACz**, the present work introduces a novel molecular framework of SAMs for TPSCs. By incorporation of two electron-donating units, TPA and DTP were conjugated in a linear structure to facilitate efficient charge transfer and then were end-capped with **PA** or **CA** anchoring groups. Notably, the molecular frameworks of all four new SAMs are well-conjugated [50,51]. To further modify the commonly studied carbazole unit to be more planar, the two phenyls in carbazole are replaced with two thiophenes for the first time to transform the carbazole to dithienopyrrole, which was then employed as a second electron donative unit in the new SAM's skeleton. The DTP core features a fused ring system comprising 5-membered heteroaromatic rings (pyrrole and thiophene) linked to an *N*-substituted phenyl ring, all residing in a more planar configuration with better π-conjugation extension. As envisioned, the triphenylamine (TPA) unit drives the hole toward the dithienopyrrole (DTP) unit and subsequently to the anchoring end (**PA** or **CA**). To optimize the electronic properties and enhance the solubility of the self-assembled monolayer (SAM) molecules, alkyl groups were introduced, resulting in distinct molecular structures. It is anticipated that SAMs with shorter chains may exhibit low solubility, leading to poor molecular packing, while SAMs with bulkier chains could reduce dye loading and hinder charge transport. To address this, dithienopyrrole cores with $^{b}C_8H_{17}$ and $^{b}C_{16}H_{33}$ chains, referred to as **DTP** and **DTP′**, respectively have been explored, aiming to achieve a balance between molecular solubility and surface packing in the SAMs for TPSCs. The extended π-conjugation system and strong π-π interactions, combined with the robust binding affinity between the functional groups (phosphonic acid and carboxylic acid) and the metal oxide surface, contributed to the formation of densely packed and well-ordered SAMs. As anticipated, the electron push-push-pull **DTP-PA (1)** SAM on the NiOx hole transport layer (HTL)/Sn-perovskite interface delivers a PCE of 8.7% with a long-term stability exceeding 3600 h. This is attributed to the superior charge transport and extraction abilities, reduced charge recombination and stronger chemical bonding of the **PA** unit compared to the **CA** unit. This marks the best result ever reported for SAM/NiOx-based TPSCs.

2. Results and discussion

2.1. Synthesis

The synthesis methods for the four new SAMs are shown in Scheme 1. The dithienopyrrole cores (**5**; R = $^{b}C_8H_{17}$, and **5′**; R = $^{b}C_{16}H_{33}$) were first synthesized from the reaction of 3,3′-dibromobithiophene with 4-alkoxyaniline in the presence of Pd-catalyst and dppf was carried out in refluxing toluene (yield 74%). Next, mono-formylation of DTPs (**5**/**5′**) under Vilemeier-Haack reaction conditions gives aldehydes **6**/**6′**, which were subsequently brominated to afford 6-bromo-alkylated phenyl-dithienopyrrole-2-carbaldehydes **7**/**7′**. The brominated aldehydes were then Stille-coupled with a triphenylamine-tin compound to give TPA functionalized dithienopyrrole-2-carbaldehydes **8**/**8′**. Finally, the latter was subjected to Knovenagel condensation reaction with cyanophosphate in presence of piperidine to give diethyl cyanophosphate compounds **9**/**9′**, which were followed by hydrolysis with trimethylsilyl bromide to yield **DTP-PA** (**1**) and **DTP′-PA** (**2**), respectively. Similarly, compounds **8**/**8′** were subjected to Knovenagel condensation reaction with cyanoacetic acid in the presence of ammonium acetate to give **DTP-CA** (**3**) and **DTP′-CA** (**4**), respectively. The detailed synthetic procedures for the new SAMs are provided in the Supporting Information. All intermediates and final compounds were comprehensively characterized using ^{1}H NMR, ^{13}C NMR, ^{31}P NMR spectroscopy, and mass spectrometry (HRMS) analysis as shown in Figs. S1-S18. The four SAMs exhibit better solubility in common organic solvents, facilitating their use for device fabrication through solution process.

To estimate the thermal behavior of the SAMs thermogravimetric analysis (TGA) was conducted (Fig. S19), and the pertinent data are presented in Table 1. The **PA**-anchored SAMs **1** and **2** demonstrate notable higher decomposition temperatures (T_d at 5% weight loss) at or above 340 °C in TGA. In contrast, the **CA**-anchored SAMs **3** and **4** show lower T_d of 188 °C and 212 °C, respectively. Additionally, the melting temperatures, measured using a melting point apparatus, reveal phase transition temperatures for these SAMs to be approximately 90–120 °C. Both sets of findings collectively suggest that these new SAMs exhibit robust thermal stability and possess a low level of crystallinity while maintaining excellent thermal stability and operational feasibility. To analyse the optical behavior of these SAMs, absorption spectra in *o*-dichlorobenzene (DCB) were recorded for all SAMs, as shown in Fig. 2a and values are summarized in Table 1. The first absorption peaks for all SAMs are located at approximately 365 nm due to the π–π* transitions of

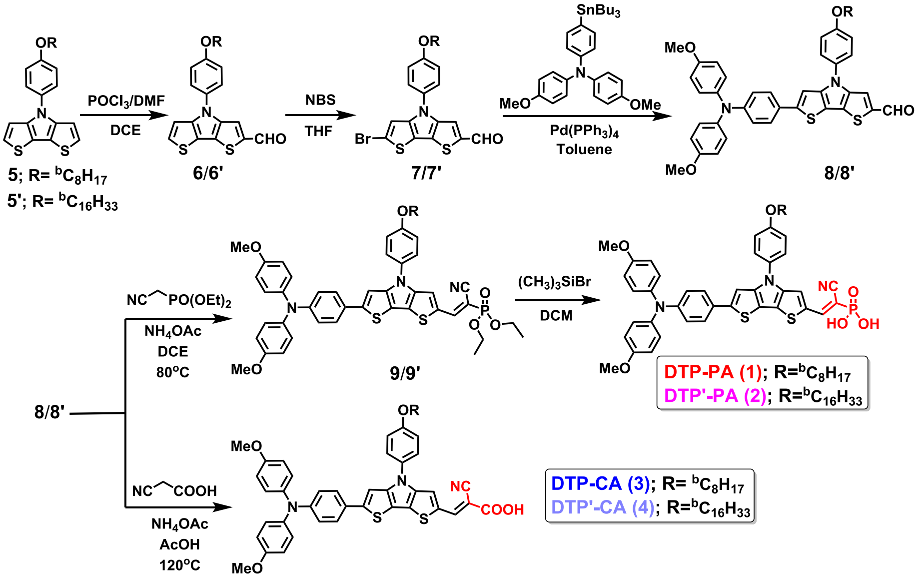

Scheme 1. Reaction pathways of target organic SAM molecules (**1–4**).

Table 1
Photophysical, electrochemical and Thermal properties of all SAMs.

SAMs	T_d [°C][a]	T_m [°C][b]	λ_{abs}[c] [nm]	λ_{onset}[d] [nm]	E_{Ox} [V][e]	HOMO [eV]		LUMO [eV]		ΔE_g [eV][g]	ΔE_g [eV][h]
						DPV[e]	DFT[f]	DPV[e]	DFT[f]		
DTP-PA (1)	337.2	120.7	365, 490	600	0.8	−5.24	−4.74	−3.18	−2.24	2.06	2.50
DTP′-PA (2)	342.7	108.6	365, 490	601	0.8	−5.24	−4.74	−3.18	−2.26	2.06	2.48
DTP-CA (3)	188.4	110.6	368, 538	630	0.82	−5.26	−4.77	−3.30	−2.40	1.96	2.37
DTP′-CA (4)	212.6	92.6	368, 538	630	0.85	−5.29	−4.77	−3.32	−2.40	1.97	2.37

[a] Thermal decomposition temperature determined by TGA.

[b] Melting temperature measured using melting point apparatus.

[c] By absorption spectra in dichlorobenzene solutions.

[d] Onset absorption.

[e] By DPV in o-$C_6H_4Cl_2$, E_{ox} = Oxidative potential; Potentials are described relative to the ferrocene internal standard (at +0.64 V); $E_{HOMO} = -(4.44 + E_{ox})$ vs. NHE; E_{LUMO} estimated from $E_{HOMO} + E_g$.

[f] By DFT calculations.

[g] Calculated optical band gap using $1240/\lambda_{onset}$.

[h] Energy band gap determined by DFT.

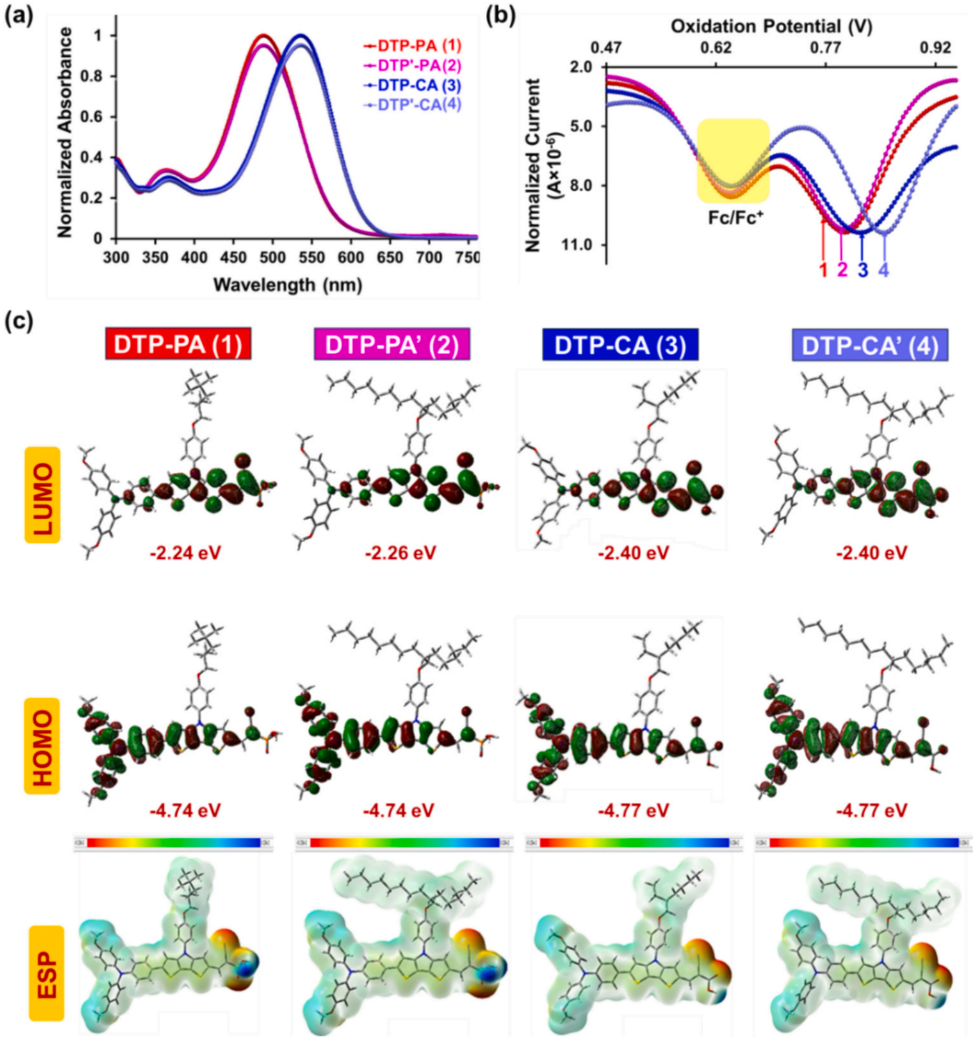

Fig. 2. (a) Normalized UV–Vis absorption spectra for all SAMs (**1–4**) in DCB; (b) Differential pulse voltammograms (DPV) for SAMs **(1–4)** recorded in o-$C_6H_4Cl_2$ with ferrocene used as the internal standard calibrated at +0.64 V; (c) DFT-derived frontier molecular orbitals and electrostatic surface potential (ESP) mapping of SAMs **(1–4)**.

the SAMs. The longer absorption wavelength is observed around 490 nm for both **DTP-PAs**. Notably there is no alkyl chain effect on absorption in both **PA**-SAMs (**1** and **2**). Similar trend was obtained for both **CA-** SAMs and absorption wavelengths were observed around 538 nm. For comparison, a 50 nm red shift of absorption maximum for both **DTP-CAs** vs **DTP-PAs**. This can be explained by the fact that the **CA** anchoring group exhibits stronger electron withdrawing nature than the **PA** anchoring group.

To investigate the electrochemical behavior of all the SAMs, the cyclic voltammetry experiments were conducted, and consecutive cycles were recorded for each SAM. The oxidation potentials of SAMs were determined in *o*-dichlorobenzene solution with Bu_4NPF_6 as supporting electrolyte, calibrated against ferrocene as internal standard set at +0.64 V (vs NHE) [52,53]. During continuous CV sweep measurements over 20 cycles (Fig. S20), all SAMs shows reversible oxidation peak and presented better electrochemical stability, making it more favorable for operational stability in TPSC devices. A Differential pulse voltammogram (DPV) was also measured to determine the precise oxidation value of all SAMs (Figs. 2b and S21). SAMs (1–4) displayed oxidation potentials of +0.8, 0.8, 0.82 and 0.85 V, respectively (Table 1). The HOMO energy level of each SAM vs NHE is estimated by using the equation $E_{HOMO} = -(4.44 + E_{ox})$. The HOMO values of **DTP-PA** (**1**) and **DTP′-PA** (**2**) are identical at −5.24 eV and no alkyl chain influence on oxidation in both PAs. For comparison of **CA**s vs **PA**s, both **CA**s (**DTP-CA** (**3**) at −5.26 eV and **DTP′-CA** (**4**) at −5.29 eV) are more down shifted than the **PA**s. As expected, with weaker electron-withdrawing **PA** unit anchored, the TPA units in **PA**s (**1** & **2**) possess higher electron density, are easier to be oxidized, and thus both **PA**s with higher HOMOs. To estimate the LUMO values of the SAMs, the HOMO energies were added to the band gap values derived from the absorption spectral onsets ($E_{LUMO} = E_{HOMO} + E_g$), resulting in −3.18, −3.18, −3.30 and −3.32 eV for **1–4**, respectively. All SAMs have HOMOs and LUMOs within a suitable energy range, enabling efficient hole extraction and electron blocking [46].

Density functional theory (DFT) calculations were performed using Gaussian09W software with the B3LYP/6-31G(d,p) basis set to study the structural and electronic properties of the SAMs (Figs. 2c). The HOMOs of **DTP**-based SAMs (**1–4**) are mainly concentrated at the donor triphenylamine and delocalized throughout the molecular backbone, attributed to the improved coplanarity of the SAMs. In contrast, the LUMOs of the SAMs are mainly localized at the **PA** or **CA** units of acceptor, with some delocalized units partially overlapping the central core which may favor hole extraction and transport. It is noteworthy that the trend of HOMO (**1**–**2 > 3**–**4**) and energy gap of all the four SAMs derived from experimental photophysical/electrochemical measurements are consistent with those obtained from DFT calculation. The DTP core, with its heteroatom substitutions, offers more efficient charge transport compared to the carbazole core, while its chemical inertness and structural rigidity enhance device stability. Furthermore, comparing **DTP-PA** with reported **GM-4PACz**, DFT calculations reveal that the HOMO level of **GM-4PACz** is more deeply shifted (−4.88 eV) than that of **DTP-PA** (−4.74 eV). As anticipated, the triphenylamine (TPA) units in DTP-based SAMs exhibit higher electron density and are more readily oxidized, resulting in HOMO levels that are consistently higher than that of **GM-4PACz**. The electrostatic potential surfaces (ESP) of the SAMs were calculated (Fig. 2c) to enhance our understanding of molecule charge distribution and identify potential interaction sites with the

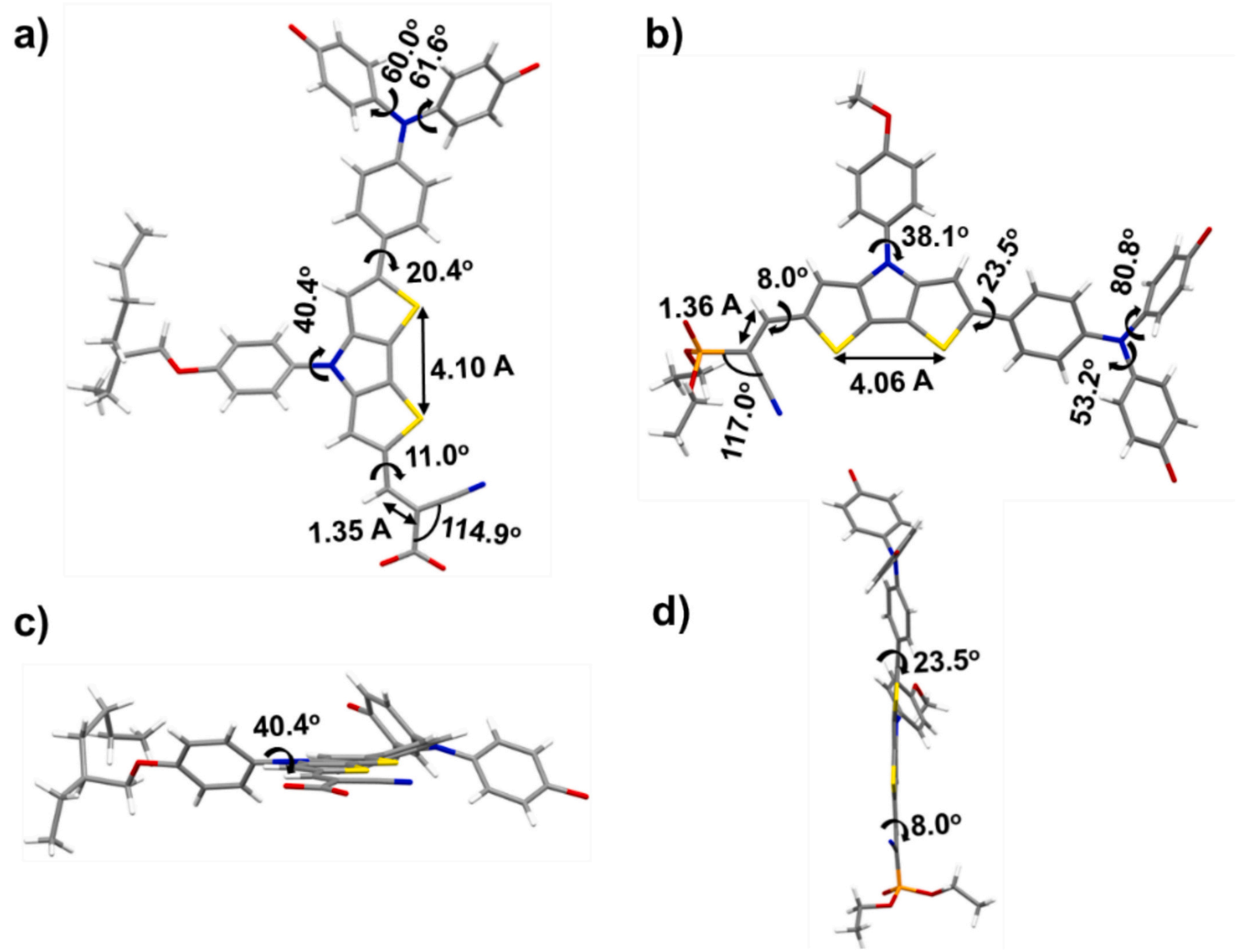

Fig. 3. Crystal structure of SAMs **DTP-CA** (**3**) and **DTP-PE** (**1-OMe**) obtained from the solvent evaporation method; (a-b) Top views of **DTP-CA** and **DTP-PE (1-OMe)** molecules with various interplanar angles in stick model, respectively (Note, OMe were omitted for clarity in triphenylamine and the colors show red for oxygen, blue for nitrogen, yellow for sulfur, and orange for phosphorus); (c-d) side views of **DTP-CA** and **DTP-PE (1-OMe)** molecules in stick models, respectively.

NiOx/ITO surface. The electron density predominantly resides on the acceptor units of **PA** or **CA**, raising a conducive environment for robust interaction between the end groups and the NiOx/ITO surface, thereby promoting the formation of a self-assembled monolayer. Note, that the tridentate mode of the **PA** anchoring group in SAMs with wider energy band gap indicates that it can be more easily anchored onto the ITO surface than the bidentate **CA** anchoring group.

2.2. Single crystal structure

Numerous attempts to grow the crystal of **DTP-PA** (**1**) have been tried, however, these efforts were not successful yet up today. In contrast, single crystals of **DTP-CA** (**3**) and **DTP-PE** (**1-OMe**) were successfully obtained through slow solvent evaporation of a dichloromethane (CH_2Cl_2) solution in hexanes environment, which enabled us to gain structural insights relevant to the self-assembled monolayers (SAMs). The structures of both molecules are illustrated in Figs. 3, S22 and S23, with the corresponding crystal parameters provided in Tables S1 and S2. Both SAMs **DTP-CA** (CCDC deposit number: 2360416) and **DTP-PE** (**1-OMe**) (CCDC deposit number: 2363614) crystallizes in a triclinic P-1 space group. As depicted in Fig. 3a, the short C═C bond length of 1.35 Å between the thiophene and **CA** groups, along with the small interplanar angles (20.4° for the **TPA** phenyl and 11.0° for the **CA** relative to the **DTP** core), suggests strong π-conjugation, facilitating efficient charge transport. In contrast, larger interplanar angles (60.0° and 61.6° for the *N*-phenyl rings on the **TPA**, and 40.4° for the phenyl ring on the **DTP** core as shown in Figs. 3c and S22b), increase solubility, enabling solution-based fabrication of high-quality films, and enhancing device PCE. For the **PE** (**1-OMe**) system, the **DTP** core and phosphorate anchoring group exhibit a planar arrangement, with an interplanar angle of 8.0°, compared to 11.0° for the **DTP** core and **CA** (Fig. 3b). The small interplanar angle of 23.5° between the **TPA** phenyl and **DTP** core, and the 8.0° angle between the **DTP** core and phosphorate group (Fig. 3d), confirm strong π-conjugation, facilitating effective charge

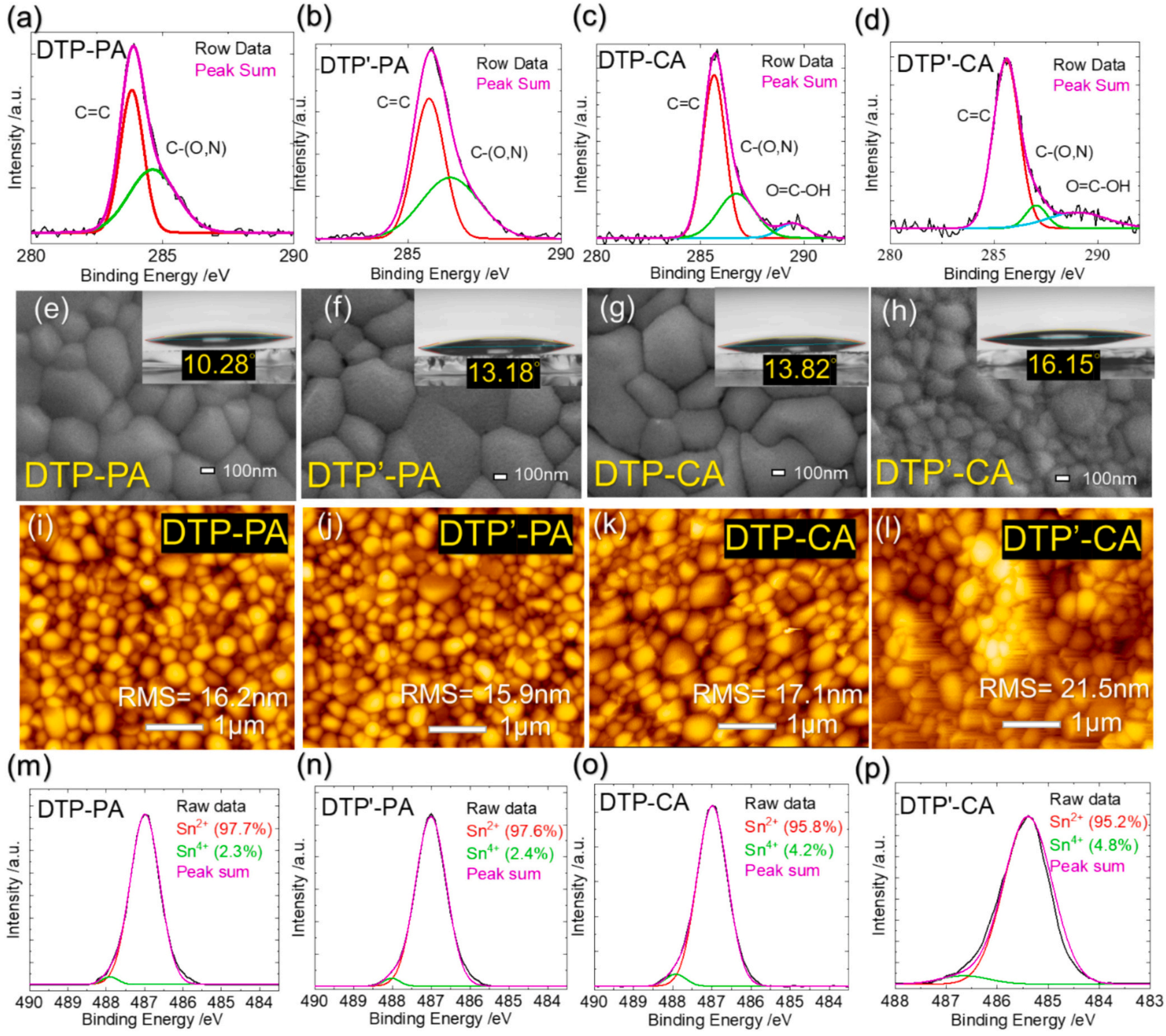

Fig. 4. XPS spectra of carbon with corresponding deconvoluted components for the ITO/NiOx substrates with SAMs (a) **DTP-PA**, (b) **DTP′-PA**, (c) **DTP-CA**, and (d) **DTP′-CA**; (e-h) SEM images of tin perovskites on varied NiOx/SAM surfaces and contact angles of SnI_2 precursor deposited on varied NiOx/SAM surfaces; (i-l) AFM images of tin perovskites deposited on varied NiOx/SAM surfaces as indicated; (m-p) XPS spectra of tin showing the Sn^{2+}/Sn^{4+} proportions in $FASnI_3$ on varied NiO_x/SAM layers.

transport from the **DTP** core to the **PE** anchoring groups. Additionally, short intramolecular distances of 2.67 Å (S—H) and 2.69 Å are observed between the **TPA** and **DTP** core for **DTP-CA** and **DTP-PE** (**1-OMe**), respectively (Figs. S22a and S23a). This planar configuration promotes a dense, tilted and well-organized one-dimensional monolayer on the substrate.

The XPS of Ni spectra features observed for both the DTP-PA-modified NiOx and the pristine NiOx film, as illustrated in the Figs. S24 and S25 below, reveal a markedly higher presence of Ni^{3+} species in the DTP-PA-incorporated NiOx layer compared to the NiOx-only counterpart. This enhancement in Ni^{3+} concentration upon the introduction of the DTP-PA self-assembled monolayer (SAM) suggests a significant alteration in the electronic structure of the NiOx surface. Given that Ni^{3+} species are known to contribute to improved p-type conductivity and enhanced hole transport, this finding implies that the SAM modification not only alters the chemical environment of NiOx but also enhances its functionality as a hole transport layer [54]. Such an increase in Ni^{3+} content is likely to facilitate more efficient hole extraction and transport at the interface, thereby contributing positively to the overall device performance in perovskite solar cells. In this study, we investigated the interaction between DTP-PA and the NiOx surface using FTIR spectroscopy. As shown in Fig. S26, the P═O stretching vibration exhibited a redshift of about 2 cm^{-1} after DTP-PA was applied to NiOx, indicating chelation between the phosphoryl group and nickel atoms on the surface. In contrast, the C—N stretching vibration remained unchanged compared to pure DTP-PA, suggesting that the interaction is specific to the P═O site. These results confirm that DTP-PA anchors selectively through its phosphoryl group, forming a stable coordination with the NiOx surface [55]. The X-ray photoelectron spectroscopy (XPS) of each sample, as shown in Fig. 4a-d, confirms the attachment of SAMs on NiOx. The spectra reveal distinct features corresponding to specific functional groups, such as C═C, C—N, and C—O. Notably, the -COOH group is detected only in the **DTP-CA** and **DTP′-CA** samples. Subsequently, a tin perovskite layer was applied to the SAM-covered substrates using the two-step procedure. The incorporation of NiOx mostly oxidizes the tin perovskite at the base, impeding hole extraction. Fig. 4e-h depict the wettability of SnI_2 solution and the morphology of FASnI3 on NiOx/SAMs (**1–4**). Initially, NiOx/SAMs were deposited onto ITO using a liquid immersion technique, with the goal of enhancing the surface hydrophilicity of NiOx. Fig. S27a-d presents the contact angles of the SnI_2 precursor solution on the SAM films: 12.71° for **DTP-PA**, 12.87° for **DTP′-PA**, 18.2° for **DTP-CA** and 24.24° for **DTP′-CA**. The functionalization of NiOx with SAMs markedly decreased the contact angles to 10.28° for **DTP-PA**, 13.18° for **DTP′-PA**, 13.82° for **DTP-CA**, and 16.15° for **DTP′-CA**, as illustrated in the insets of Fig. 4e-h. This surface modification promotes further FAI deposition, resulting in formation of $FASnI_3$ perovskite with desirable morphologies. Enhanced hydrophilicity suggests a relationship between the SAMs processability and their performance in devices, with improved device performance observed only with SAMs exhibiting optimal processability. Among the four SAMs, NiOx/**DTP-PA** showed smaller contact angles than NiOx/**DTP′-PA**, NiOx/**DTP-CA** and NiOx/**DTP′-CA**, indicating its superior wettability and processability. To evaluate the surface hydrophobicity of the perovskite films, we performed water contact angle measurements on tin perovskite layers deposited atop various SAMs as shown in Fig. S28. Notably, the perovskite film fabricated on the **DTP-PA**-modified NiOx substrate exhibited a significantly larger contact angle—exceeding 50°—compared to other configurations. This elevated contact angle is indicative of enhanced surface hydrophobicity, suggesting that the presence of the PA (phosphonic acid) anchoring group contributes to a more water-repellent interface. The improved water resistance can be attributed to the molecular structure of the **DTP-PA** SAM, which effectively passivates the NiOx surface and reduces its affinity for moisture. Consequently, the **NiOx/DTP-PA/$FASnI_3$** interface offers better protection against water-induced degradation, which is particularly beneficial for the long-term stability of tin-based perovskite solar cells. This result supports the role of interfacial engineering, not only in optimizing charge transport but also in enhancing environmental stability through moisture suppression. Based on the contact angle measurements, it can be inferred that phosphonic acid (PA) possesses a phosphonate group capable of forming a tridentate bonding configuration with the substrate surface. This stronger and more extensive interaction leads to a smaller contact angle compared to carboxylic acid (CA), which typically forms only bidentate interactions. The reduced contact angle indicates improved surface wetting and stronger molecular anchoring, both of which are beneficial for creating a more uniform and compact perovskite film during fabrication. Consequently, the use of PA-based self-assembled monolayers (SAMs) is more suitable for perovskite solar cell applications, as this enhanced interfacial interaction contributes to better film morphology and ultimately results in superior device performance.

Scanning electron microscopy (SEM) and atomic force microscopy (AFM) were used to examine the morphologies of tin perovskite films deposited on varied NiOx/SAMs. Fig. 4e-h illustrates the morphology of $FASnI_3$ on NiOx/SAMs, with the DTP-PA film (Fig. 4e) exhibiting more homogeneous crystals relative to the other films. The AFM data presented in Fig. 4i-l substantiate this discovery, as they were utilized to evaluate the surface roughness of the tin perovskites on various NiOx/SAMs films. The AFM images indicate that perovskites formed on **DTP-PA** exhibited lower surface roughness compared to the other SAMs. AFM images of SAMs applied to ITO and NiOx/ITO substrates are shown in Figs. S29 and S30, respectively. The roughness of the bare ITO surface results in the random distribution of SAM molecules (Figs. S29a-d). When NiOx was applied to the ITO substrate, it modified the surface roughness, resulting in a flatter appearance in the corresponding AFM images (Figs. S30a-d). This highlights the role of the NiOx layer in improving film hydrophilicity and filling gaps on the ITO substrates.

Figs. S29 and S30 show KPFM images of the surface acoustic microscopy tests performed for SAMs deposited on ITO (Fig. S29e-h) and NiOx/ITO (Fig. S30e-h) substrates. The surface roughness and potentials of ITO with SAMs **1–4** are 3.8 nm, 4.85 nm, 3.19 nm, 3.25 nm and 3.95 mV, 3.06 mV, 5.16 mV, 5.04 mV, respectively, while the NiOx/ITO with SAMs **1–4** are 5.11 nm, 6.46 nm, 4.33 nm, 4.09 nm and 2.39 mV, 3.05 mV, 5.08 mV, 5.25 mV respectively. Significantly, perovskites utilizing NiOx/DTP-PA demonstrated a reduced surface potential compared to the alternatives. ITO/SAM were sheet-like, while ITO/NiOx/SAM substrates were dense and spherical. This structural modification significantly enhances the particular area of surface of the latter, facilitating a compact and uniform layer between the NiOx/ITO substrate and $FASnI_3$.

The side-view SEM images (Fig. S31) depict the perovskite film thicknesses on various NiOx/SAM films. The film of perovskite on NiOx/**DTP-PA** exhibited larger and more uniform crystal grains with larger film thickness compared to the other films.

Fig. 4m-p illustrates the X-ray Photoelectron Spectroscopy (XPS) analysis of Sn 3d peaks, comparing the ratios of Sn^{2+} (active state) and Sn^{4+} (oxidized state) for various DTP-based SAM-modified surfaces. **DTP-PA** demonstrates the best passivation performance with 97.7% Sn^{2+}, closely followed by **DTP′-PA** with 97.6% Sn^{2+}. In contrast, **DTP-CA** and **DTP′-CA** exhibit lower Sn^{2+} proportions at 95.8% and 95.2%, respectively, with higher Sn^{4+} content, indicating reduced stabilization of Sn^{2+}. The superior performance of PA-based SAMs is attributed to their stronger and more uniform interfacial bonding, which effectively prevents Sn oxidation by passivating surface defects and shielding the material from environmental factors like oxygen and moisture. These results highlight the importance of molecular design, with PA-based SAMs offering better electronic properties, reduced trap-assisted recombination, and improved interfacial quality, all critical for achieving higher efficiency and stability in TPSCs. SAM functionalization of NiOx markedly reduces the Sn^{2+}/Sn^{4+} oxidation, with the **DTP-PA** sample showing the highest Sn^{2+}/Sn^{4+} ratio. These findings underscore the critical role of SAM side chains in the development of high-quality perovskite layers, particularly highlighting that the perovskite film formed with the intermediate-sized alkyl chain (**DTP-PA**) produce superior quality of the perovskite layer.

As shown in Fig. S32, the X-ray diffraction (XRD) of tin perovskites reveals enhanced crystallization intensity when the perovskites were deposited on SAMs with NiOx. NiOx oxidizes SnI_2 as an isolated hole transport layer, reducing tin perovskite crystallinity, especially in the (100) facet. The hole-extraction of $FASnI_3$ on various SAMs were evaluated using the TCSPC, which were performed using a 635 nm picosecond-pulse laser with a full width at half maximum (FWHM) of approximately 110 ps, indicating an instrument response function (IRF) of 110 ps. As shown in Fig. 5a, all decay profiles were clearly shown in a semilogarithmic scale, with time constants much greater than the temporal resolution of 110 ps. Some decay profiles exhibited higher background levels; this was attributed to the scattering of the pump pulse. To minimize scattered light, a 720 nm long-pass filter was employed during the measurements. The data were only normalized to the peaks without any further manipulation. The decay profiles were examined utilizing a bi-exponential function model, with the fitted parameters presented in Table S3. The results demonstrate that the ability of hole-extraction follows the order: NiOx/**DTP-PA** (1.2 ns) > NiOx/**DTP′-PA** (1.5 ns), >NiOx/**DTP-CA** (1.6 ns), and NiOx/**DTP′-CA** (3.6 ns).

We performed space-charge-limited current (SCLC) measurements again by using hole-only device structures with the configuration ITO/NiOx/DTP-SAM/tin perovskite/PTAA/Ag as shown in Fig. S33 and Tables S4-S7. To accurately identify the charge transport behavior, we plotted the current–voltage characteristics on a log–log scale, which clearly distinguishes three distinct regions: the ohmic region at low voltages, the trap-filled limit (TFL) region characterized by a sharp increase in current, and the trap-free Child's regime (SCLC region), where the current scales quadratically with voltage. To evaluate the hole mobility, we focused specifically on the trap-free region and applied the Mott–Gurney law, which allows us to extract mobility values under conditions where trap states are assumed to be fully occupied and no longer affect charge transport. Among the various self-assembled monolayers (SAMs) tested, the device incorporating NiOx/DTP-PA exhibited a noticeably lower trap-filled limit voltage, indicating a significantly reduced trap density within the active layer. Using the Mott–Gurney law, we plotted the product of current density (J) and the cube of the film thickness (L^3) against the square of the applied voltage (V^2) to determine the hole mobility from the slope of the JL^3–V^2 curve. The results indicate that the NiOx/DTP-PA device exhibits superior hole mobility relative to the other SAM-modified counterparts. This combination of lower trap density and enhanced charge transport strongly suggests that NiOx/DTP-PA serves as an effective interfacial layer for hole injection and transport. As a result, the NiOx/DTP-PA-based device not only demonstrates superior electrical properties but also achieves the best overall photovoltaic performance among the SAM variants studied, confirming its potential as an optimized hole transport layer for tin-based perovskite solar cells.

Space-charge limited current (SCLC) measurements were conducted for the *J-V* scans under dark condition. The device structure used for the SCLC measurements is given as ITO/NiOx/SAM/$FASnI_3$/Al, and data were analyzed according to Mott-Gurney equation [56–58]:

$$J = \frac{9}{8}\varepsilon_0\varepsilon_r\mu\frac{V^2}{L^3} \tag{1}$$

where J is current density, ε_0 is the vacuum permittivity, ε_r is the relative permittivity, V is applied voltage, L is the thickness of the SAM film, and μ is the hole mobility. The plots of $J{*}L^3$ vs V [2] will give the slope which contains the information of hole mobility (μ). The SCLC of NiOx/SAM thin films shows that NiOx/**DTP-PA** has the maximum hole mobility (Fig. 5b) among all samples, indicating its superior performance than

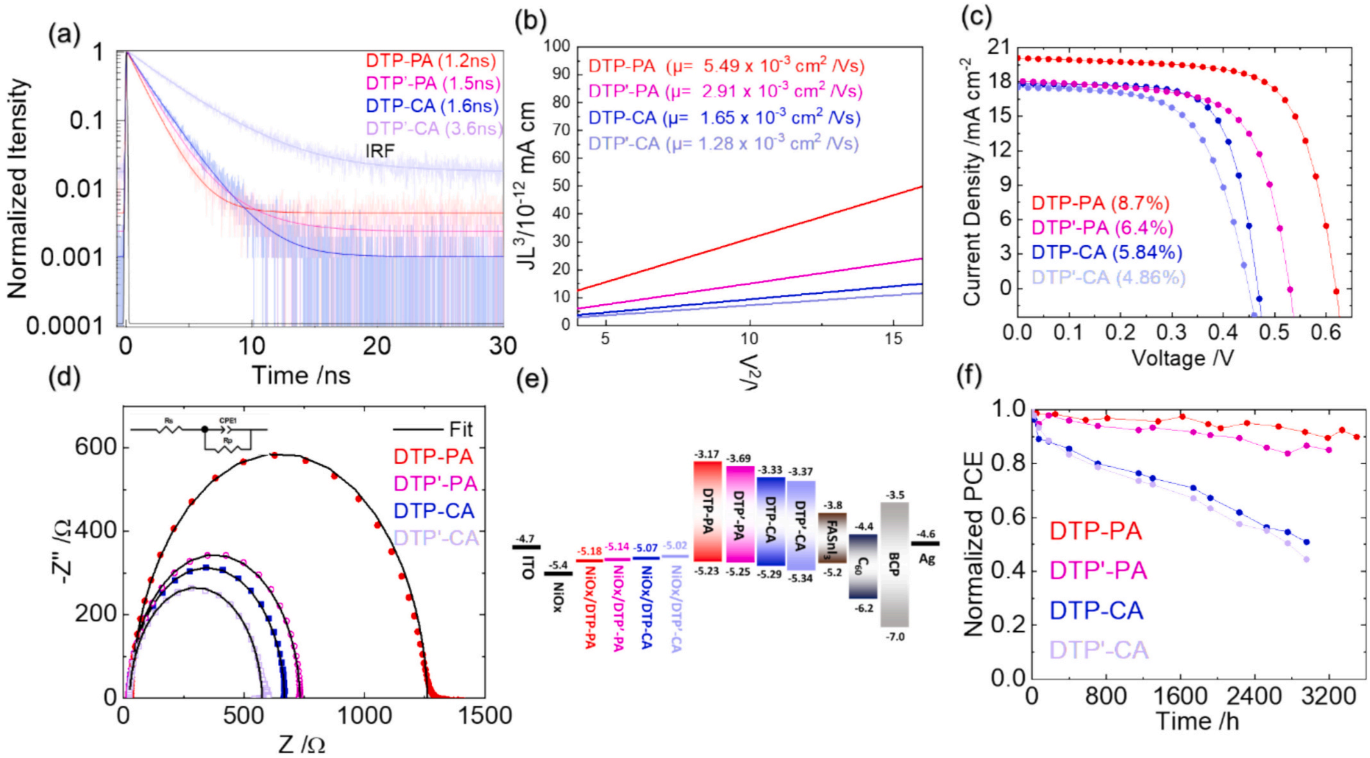

Fig. 5. (a) PL decay profiles measured using time-correlated single-photon counting (TCSPC) excited at 635 nm with an instrument response function of FWHM ~110 ps; (b) space-charge limited current (SCLC) of $FASnI_3$ on NiOx/SAMs as indicated (the raw data are shown as symbols and the solid traces are shown as fitting results) with the structure of ITO/NiOx/SAM/$FASnI_3$/Al; (c) *J-V* curves of TPSCs with NiOx functionalized by varied SAMs, measured in fresh devices; (d) electrochemical impedance spectroscopy (EIS) Nyquist plots for the devices made of $FASnI_3$ deposited on NiOx/SAMs as indicated under V_{OC} in the dark (the raw data are shown as symbols and the solid curves are shown as fitting results); (e) energy-level diagram determined from UPS and absorption spectra; (f) long-term stability tests of unencapsulated devices with NiOx/SAMs, stored in the glove box.

other SAMs.

Two steps were used to make TPSC devices, featuring a layered structure of ITO/NiOx/SAM/$FASnI_3$/C60/BCP/Ag. Fig. 5c shows the current-voltage (*J*-*V*) characteristics of the NiOx/SAM devices, with performance following the trend: **DTP-PA** (8.7%) > **DTP′-PA** (6.4%) > **DTP-CA** (5.8%) > **DTP′-CA** (4.9%). Detailed photovoltaic parameters are provided in Table S8. The performance order depicted in Fig. 5c corresponds to the morphological and passivation of the SAM molecules. Devices incorporating NiOx with **DTP′-PA**, **DTP-CA**, and **DTP′-CA** exhibited reduced efficiency attributable to their poor morphology, as illustrated by the SEM and AFM (Fig. 4e-l) images. The notable efficiency (PCE = 8.7%) of NiOx/**DTP-PA** device is due to its high film quality (Fig. 4e/i), fast hole extraction and improved hole mobility (Fig. 5a and b). The UV–vis absorption and photoluminescence (PL) spectra of perovskite films prepared via varied SAMs, displayed in Fig. S34, show no significant differences between these molecules. The IPCE spectroscopy for the NiOx/SAM devices, illustrated in Fig. S35, together with the integrated short-circuit current densities (JSC), further validate the J-V curve results (Fig. 5c). The results highlight the remarkable JSC value of the NiOx/DTP-PA device, corresponding with its IPCE response in the 350–700 nm spectrum range, as illustrated in Fig. S31.

Electrochemical impedance spectroscopy (EIS) measurements were conducted in the dark at the V_{OC} value to examine the charge recombination characteristics of the NiOx/SAM TPSCs. The Nyquist plots of all devices displayed in Fig. 5d show a single semicircle pattern. The charts were examined utilizing a simple RC equivalent circuit model to precisely interpret the EIS data (see supporting information). The fitted impedances indicate the charge recombination resistances, which follow to the following order: NiOx/**DTP-PA** > NiOx/**DTP′-PA** > NiOx/**DTP-CA** > NiOx/**DTP′-CA**, matching the trend observed in the V_{OC} values shown in Fig. 5c. This study highlights the superior performance of the NiOx/**DTP-PA** device, which exhibits the highest V_{OC} among all other devices.

The energy level of the SAM with and without NiOx was analyzed using ultraviolet photoelectron spectroscopy (UPS) and DPV. Figs. S36 and S37 display the UPS without and with NiOx layer, respectively. Fig. 5e illustrates the energy-level for SAM devices, inclusive of both NiOx-modified and non-modified variants. The findings indicate that NiOx/SAM exhibit elevated HOMO levels relative to those without NiOx, which is crucial for the hole transport from $FASnI_3$ to the NiOx/SAM. Notably, the HOMO of the NiOx/**DTP-PA** film closely aligns with that of $FASnI_3$, supporting the superior device performance shown in Fig. 5c. The long-term stability of various NiOx/SAM TPSCs, as illustrated in Fig. 5g, shows a consistent decline in performance over 3600 h. The NiOx/**DTP-PA** device demonstrated remarkable stability, retaining nearly 80% of its initial efficiency after 3600 h. This longevity is attributed to the device's excellent performance as reported previously. To further validate the reproducibility of our device fabrication approach, we conducted statistical analyses over 15 independently fabricated devices for each SAM-modified NiOx configuration. As shown in Fig. S38 and Tables S9–S12, the NiOx/DTP-PA-based devices exhibited the highest average power conversion efficiency (PCE), with minimal batch-to-batch variation, highlighting their excellent reproducibility. In contrast, devices employing DTP′-PA, DTP-CA, and DTP′-CA SAMs showed lower average efficiencies, with correspondingly higher standard deviations. These results not only demonstrate the superior performance of the DTP-PA SAM but also underscore its advantage in delivering uniform device quality across multiple fabrication batches. Additionally, the NiOx/**DTP-PA** device showed negligible hysteresis shown in Fig. S39. The unencapsulated NiOx/**DTP-PA** device maintained over 90% PCE at the maximum power point (MPP) for 5 h (Fig. S40), further demonstrating its outstanding stability under light-soaking condition. The effects of NiOx in our study have been thoroughly investigated, and Fig. S41 provides a clear comparison between devices using only SAMs (without NiOx) and those incorporating the NiOx layer. As shown in the figure, the devices with SAMs alone exhibit significantly lower power conversion efficiencies (PCEs), with DTP-PA-only and DTP-CA-only devices achieving 4.16% and 3.22%, respectively, while DTP′-PA-only and DTP′-CA-only devices show even lower efficiencies at 3.81% and 1.28%, respectively. These values are notably lower than the corresponding NiOx/SAM-based devices. This study highlights the crucial role of the NiOx interlayer in enhancing the performance of the SAMs devices by promoting the formation of a robust and uniform perovskite layer, which improves the overall performance of the SAM devices in this series. Among the four SAM molecules with varying alkyl side chains and anchoring groups, **DTP-PA**, with its medium chain length and cyano phosphonic acid as an anchoring group, was found to facilitate the subsequent fabrication of a perovskite layer with superior crystal morphology, reduced film roughness, improved crystallinity, retarded charge recombination, enhanced hole mobility, and better hole extraction ability compared to the other SAMs. We also measure the NiOx and PEDOT:PSS device. The performance of two-step-processed TPSCs based on NiOx and PEDOT:PSS are inferior to those employing NiOx/SAMs as the hole transport layer as shown in Figs. S42 and S43.

Fig. S44 presents the results of light intensity-dependent measurements on four types of perovskite solar cells using different self-assembled monolayers (SAMs) as the hole transport layer (HTL): DTP-PA, DTP′-PA, DTP-CA, and DTP′-CA. These measurements provide insights into recombination behavior and charge transport dynamics in these devices. The Fig. S44 shows the dependence of open-circuit voltage (Voc) on light intensity (I_{light}). According to the diode equation in the figure where the ideality factor n indicates the dominant recombination mechanism. An ideality factor closes to 1 implies bimolecular recombination, while larger values suggest trap-assisted recombination. Among the four devices, DTP-PA exhibits the lowest ideality factor ($n = 1.18$), indicating minimal trap-assisted recombination. In contrast, DTP′-CA shows a significantly higher ideality factor ($n = 4.78$), suggesting severe trap-mediated recombination likely due to poor interfacial quality. Fig. S44 displays the relationship between short-circuit current density (Jsc) and light intensity, which follows the power law in the figure. The parameter α indicates the extent of bimolecular recombination and carrier collection efficiency. A value close to 1 implies efficient charge extraction with minimal recombination losses. All four devices exhibit α values near 1, ranging from 0.911 to 0.987, suggesting that Jsc is not strongly limited by recombination under these conditions. However, the slightly lower α values in DTP-CA and DTP′-CA again hint at interfacial losses or trap states.

3. Conclusion

Four new push-push-pull type dithienopyrrole-based organic molecules, featuring two alkyl chains (branch-C_8H_{17}/$C_{16}H_{33}$ chains) and incorporating either cyano phosphonic acid (**PA**) or cyano acetic acid (**CA**) as anchoring groups, were synthesized and utilized as SAMs for TPSCs. The single crystal structures of the **DTP-CA (3)** and **DTP-PE (1-OMe)** reveal the planar nature of the core, which facilitates enhanced π-conjugation, and optimal dihedral angles, there by promoting the formation of a uniform and dense SAM on the NiOx/ITO substrate. The incorporation of dithienopyrrole-based SAMs at the NiOx/Sn-perovskite interface via a two-step spin coating technique, improved ITO hydrophilicity, surface roughness, energy level alignment, perovskite film morphology, and thickness. It also reduced charge carrier recombination, increased hole mobility, and efficient hole extraction into the HTL. Furthermore, the anchoring group plays an important role in SAMs with stronger chemical bonding of the **PA** unit compared to the **CA** unit, which results in better device performance for the former than for the latter. As far as we are aware, the TPSC device utilizing the combination of **DTP-PA (1)** SAM with NiOx HTM displayed the highest PCE of 8.7% ever reported for the non-PEDOT:PSS HTL via a two-step fabrication technique; note that traditional one-step method cannot produce high-quality tin perovskite layer on the SAM/NiOx surface. Moreover, this device demonstrated remarkable stability, maintaining over 80% of the original power conversion efficiency for approximately 3600 h without encapsulation for the device. This ED push-push SAM study offers a new approach to design novel SAM molecules for TPSC applications.

CRediT authorship contribution statement

Rajendiran Balasaravanan: Software, Methodology, Investigation, Formal analysis, Data curation, Conceptualization, Writing – review & editing, Writing – original draft. **Chun-Hsiao Kuan:** Software, Resources, Investigation, Formal analysis, Data curation, Conceptualization, Writing – review & editing, Writing – original draft. **Yun-Sheng Shih:** Software, Resources, Formal analysis, Data curation. **Hsu-Lung Cheng:** Software, Formal analysis, Data curation. **Deebakkrishnan Ganesan:** Formal analysis, Data curation. **Shao-Huan Hong:** Software, Resources, Formal analysis, Data curation. **Cheng-Liang Liu:** Software, Resources, Formal analysis, Data curation. **Yun-Rou Zhong:** Software, Resources, Methodology, Formal analysis, Data curation. **Xianyuan Jiang:** Formal analysis, Data curation. **Ming-Chou Chen:** Supervision, Project administration, Investigation, Funding acquisition, Writing – review & editing. **Eric Wei-Guang Diau:** Supervision, Project administration, Investigation, Conceptualization, Writing – review & editing.

Declaration of competing interest

The authors declare that they have no known competing financial interests or personal relationships that could have appeared to influence the work reported in this paper.

Acknowledgment

We thank the Instrumentation Center at NCU for SAMs characterization and Pei-Lin Chen (Instrumentation Center at NTHU) for Single Crystal X-ray Diffractometer analysis. We gratefully acknowledge the support by the National Science and Technology Council (NSTC), Taiwan (grant No. NSTC 112-2639-M-A49-001-ASP, NSTC 113-2639-M-A49-001-ASP, and MOST 111-2113-M-008-004-MY3), the Center for Emergent Functional Matter Science of National Yang-Ming Chiao-Tung University (NYCU) from the Featured Areas Research Center Program within the framework of the Higher Education Sprout Project by the Ministry of Education (MOE) in Taiwan. We gratefully acknowledge Drs. Y.-W. Tsai and J.-M. Lin (TPS 25A1, NSRRC) for their support with GIWAXS data analysis. We also thank Drs. B.-H. Liu and C.-H. Wang (TLS 24A1, NSRRC) for their insightful assistance with UPS and XPS analyses, and Dr. Y.-C. Lee and Ms. P.-Y. Huang (TLS 14A1, NSRRC) for their valuable help with IR data interpretation.

Appendix A. Supplementary data

Supplementary data to this article can be found online at https://doi.org/10.1016/j.cej.2025.165231.

Data availability

Data will be made available on request.

References

[1] G. Tumen-Ulzii, T. Matsushima, D. Klotz, M.R. Leyden, P. Wang, C. Qin, J.-W. Lee, S.-J. Lee, Y. Yang, C. Adachi, Hysteresis-less and stable perovskite solar cells with a self-assembled monolayer, Commun. Mater. 1 (2020) 31.

[2] N.J. Jeon, J.H. Noh, W.S. Yang, Y.C. Kim, S. Ryu, J. Seo, S.I. Seok, Compositional engineering of perovskite materials for high-performance solar cells, Nature 517 (2015) 476–480.

[3] J.J. Yoo, G. Seo, M.R. Chua, T.G. Park, Y. Lu, F. Rotermund, Y.-K. Kim, C.S. Moon, N.J. Jeon, J.-P. Correa-Baena, V. Bulovic, S.S. Shin, M.G. Bawendi, J.W. Seo, Efficient perovskite solar cells via improved carrier management, Nature 590 (2021) 587–593.

[4] M. Jeong, I.W. Choi, E.M. Go, Y. Cho, M. Kim, B. Lee, S. Jeong, Y. Jo, H.W. Choi, J. Lee, J.-H. Bae, S.K. Kwak, D.S. Kim, C. Yang, Stable perovskite solar cells with efficiency exceeding 24.8% and 0.3-V voltage loss, Science 369 (2020) 1615–1620.

[5] A. Abid, P. Rajamanickam, E.W.-G. Diau, Design of a simple bifunctional system as a self-assembled monolayer (SAM) for inverted tin-based perovskite solar cells, Chem. Eng. J. 477 (2023) 146755.

[6] N. Ahn, M. Choi, Towards long-term stable perovskite solar cells: degradation mechanisms and stabilization techniques, Adv. Sci. 11 (2024) 2306110.

[7] R. Wang, J. Zhu, J. You, H. Huang, Y. Yang, R. Chen, J. Wang, Y. Xu, Z. Gao, J. Chen, B. Xu, B. Wang, C. Chen, D. Zhao, W.-H. Zhang, Custom-tailored solvent engineering for efficient wide-bandgap perovskite solar cells with a wide processing window and low VOC losses, Energy Environ. Sci. 17 (2024) 2662–2669.

[8] A. Farag, T. Feeney, I.M. Hossain, F. Schackmar, P. Fassl, K. Küster, R. Bäuerle, M. A. Ruiz-Preciado, M. Hentschel, D.B. Ritzer, A. Diercks, Y. Li, B.A. Nejand, F. Laufer, R. Singh, U. Starke, U.W. Paetzold, Evaporated self-assembled monolayer hole transport layers: lossless interfaces in p-i-n perovskite solar cells, Adv. Energy Mater. 13 (2023) 2203982.

[9] Z. Li, X. Sun, X. Zheng, B. Li, D. Gao, S. Zhang, X. Wu, S. Li, J. Gong, J.M. Luther, Z. Li, Z. Zhu, Stabilized hole-selective layer for high-performance inverted p-i-n perovskite solar cells, Science 382 (2023) 284–289.

[10] M.A. Green, E.D. Dunlop, M. Yoshita, N. Kopidakis, K. Bothe, G. Siefer, D. Hinken, M. Rauer, J. Hohl-Ebinger, X. Hao, Solar cell efficiency tables (version 64), Prog. Photovolt. Res. Appl. 32 (2024) 425–441.

[11] F. Gu, Z. Zhao, C. Wang, H. Rao, B. Zhao, Z. Liu, Z. Bian, C. Huang, Lead-free tin-based perovskite solar cells: strategies toward high performance, Sol. RRL 3 (2019) 1900213.

[12] T.J. Macdonald, L. Lanzetta, X. Liang, D. Ding, S.A. Haque, Engineering stable lead-free tin halide perovskite solar cells: lessons from materials chemistry, Adv. Mater. 35 (2023) 2206684.

[13] W. Li, T. Mi, T. Tian, M. Yang, H. Pang, Mitigating lead toxicity in halide perovskite solar cells: strategies for sustainable development, Inorganics 13 (2025) 123.

[14] Y. Shi, Z. Zhu, D. Miao, Y. Ding, Q. Mi, Interfacial dipoles boost open-circuit voltage of tin halide perovskite solar cells, ACS Energy Lett. 9 (2024) 1895–1897.

[15] J. Chen, J. Luo, E. Hou, P. Song, Y. Li, C. Sun, W. Feng, S. Cheng, H. Zhang, L. Xie, C. Tian, Z. Wei, Efficient tin-based perovskite solar cells with trans-isomeric fulleropyrrolidine additives, Nat. Photonics 18 (2024) 464–470.

[16] J. Chen, J. Luo, Y. Li, X. Chen, Z. Song, E. Hou, C. Sun, H. Zhang, S. Cheng, Y. Xing, S. Chen, X. Zhao, L. Xie, C. Tian, Z. Wei, Spatially isomeric fulleropyrrolidines enable controlled stacking of perovskite colloids for high-performance tin-based perovskite solar cells, Angew. Chem. Int. Ed. 64 (2025) e202420150.

[17] J. Xia, V. Joseph, A.A. Sutanto, R. Balasaravanan, Y. Ezhumalai, Z.-X. Zhang, J.-S. Ni, S.T. Yogesh, S.-L. Yau, G. Shao, Z. Qiu, A.M. Asiri, M.-C. Chen, M. K. Nazeeruddin, Isomeric imidazole functionalized bithiophene-based hole transporting materials for stable perovskite solar cells, Cell Rep. Phys. Sci. 4 (2023) 101312.

[18] S.J. Lee, S.S. Shin, Y.C. Kim, D. Kim, T.K. Ahn, J.H. Noh, J. Seo, S.I. Seok, Fabrication of efficient formamidinium tin iodide perovskite solar cells through SnF2–pyrazine complex, J. Am. Chem. Soc. 138 (2016) 3974–3977.

[19] A.R.M. Alghamdi, M. Yanagida, Y. Shirai, G.G. Andersson, K. Miyano, Surface passivation of sputtered NiOx using a SAM interface layer to enhance the performance of perovskite solar cells, ACS Omega 7 (2022) 12147–12157.

[20] X. Jiang, F. Wang, Q. Wei, H. Li, Y. Shang, W. Zhou, C. Wang, P. Cheng, Q. Chen, L. Chen, Z. Ning, Ultra-high open-circuit voltage of tin perovskite solar cells via an electron transporting layer design, Nat. Commun. 11 (2020) 1245.

[21] E. Jokar, H.-S. Chuang, C.-H. Kuan, H.-P. Wu, C.-H. Hou, J.-J. Shyue, E.W.-G. Diau, Slow passivation and inverted hysteresis for hybrid tin perovskite solar cells attaining 13.5% via sequential deposition, J. Phys. Chem. Lett. 12 (2021) 10106–10111.

[22] D.S. Utomo, L.M. Svirskaite, A. Prasetio, V. Malinauskiene, P. Dally, E. Aydin, A. Musiienko, V. Getautis, T. Malinauskas, R. Azmi, S. De Wolf, Nonfullerene self-assembled monolayers as electron-selective contacts for n-i-p perovskite solar cells, ACS Energy Lett. 9 (2024) 1682–1692.

[23] S. Li, Q. Fu, L. Meng, X. Wan, L. Ding, G. Lu, G. Lu, Z. Yao, C. Li, Y. Chen, Achieving over 18% efficiency organic solar cell enabled by a ZnO-based hybrid electron transport layer with an operational lifetime up to 5 years, Angew. Chem. Int. Ed. 61 (2022) e202207397.

[24] Z. Yang, J. Dou, M. Wang, Interface engineering in n-i-p metal halide perovskite solar cells, Solar RRL 2 (2018) 1800177.

[25] H. Kim, M. Pei, Y. Lee, A.A. Sutanto, S. Paek, V.I.E. Queloz, A.J. Huckaba, K.T. Cho, H.J. Yun, H. Yang, M.K. Nazeeruddin, Self-crystallized multifunctional 2D perovskite for efficient and stable perovskite solar cells, Adv. Funct. Mater. 30 (2020) 1910620.

[26] Y. Duan, Y. Chen, Y. Wu, Z. Liu, S. Liu, Q. Peng, A comprehensive review of organic hole-transporting materials for highly efficient and stable inverted perovskite solar cells, Adv. Funct. Mater. 34 (2024) 2315604.

[27] A. Velusamy, C.-H. Kuan, T.-C. Lin, Y.-S. Shih, C.-L. Liu, D.-Y. Zeng, Y.-G. Li, Y.-H. Wang, X. Jiang, M.-C. Chen, E.W.-G. Diau, Bithiophene imide-based self-assembled monolayers (SAMs) on NiOx for high-performance tin perovskite solar cells fabricated using a two-step approach, ACS Appl. Mater. Interfaces 17 (2025) 952–962.

[28] A. Magomedov, A. Al-Ashouri, E. Kasparavičius, S. Strazdaite, G. Niaura, M. Jošt, T. Malinauskas, S. Albrecht, V. Getautis, Self-assembled hole transporting

monolayer for highly efficient perovskite solar cells, Adv. Energy Mater. 8 (2018) 1801892.

[29] L. Caliò, J. Follana-Berná, S. Kazim, M. Madsen, H.-G. Rubahn, Á. Sastre-Santos, S. Ahmad, Cu(II) and Zn(II) based phthalocyanines as hole selective layers for perovskite solar cells, Sustain. Energ. Fuels 1 (2017) 2071–2077.

[30] Q. Cao, T. Wang, X. Pu, X. He, M. Xiao, H. Chen, L. Zhuang, Q. Wei, H.-L. Loi, P. Guo, B. Kong, G. Feng, J. Zhuang, G. Feng, X. Li, F. Yan, Co-self-assembled monolayers modified NiOx for stable inverted perovskite solar cells, Adv. Mater. 36 (2024) 2311970.

[31] Y. Wang, Q. Liao, J. Chen, W. Huang, X. Zhuang, Y. Tang, B. Li, X. Yao, X. Feng, X. Zhang, M. Su, Z. He, T.J. Marks, A. Facchetti, X. Guo, Teaching an old anchoring group new tricks: enabling low-cost, eco-friendly hole-transporting materials for efficient and stable perovskite solar cells, J. Am. Chem. Soc. 142 (2020) 16632–16643.

[32] B. Dong, M. Wei, Y. Li, Y. Yang, W. Ma, Y. Zhang, Y. Ran, M. Cui, Z. Su, Q. Fan, Z. Bi, T. Edvinsson, Z. Ding, H. Ju, S. You, S.M. Zakeeruddin, X. Li, A. Hagfeldt, M. Grätzel, Y. Liu, Self-assembled bilayer for perovskite solar cells with improved tolerance against thermal stresses, Nat. Energy 10 (2025) 342–353.

[33] W.-Y. Chen, L.-L. Deng, S.-M. Dai, X. Wang, C.-B. Tian, X.-X. Zhan, S.-Y. Xie, R.-B. Huang, L.-S. Zheng, Low-cost solution-processed copper iodide as an alternative to PEDOT:PSS hole transport layer for efficient and stable inverted planar heterojunction perovskite solar cells, J. Mater. Chem. A 3 (2015) 19353–19359.

[34] S. Zhang, R. Wu, C. Mu, Y. Wang, L. Han, Y. Wu, W.-H. Zhu, Conjugated self-assembled monolayer as stable hole-selective contact for inverted perovskite solar cells, ACS Mater. Lett. 4 (2022) 1976–1983.

[35] D. Li, Q. Lian, T. Du, R. Ma, H. Liu, Q. Liang, Y. Han, G. Mi, O. Peng, G. Zhang, W. Peng, B. Xu, X. Lu, K. Liu, J. Yin, Z. Ren, G. Li, C. Cheng, Co-adsorbed self-assembled monolayer enables high-performance perovskite and organic solar cells, Nat. Commun. 15 (2024) 7605.

[36] K. Wojciechowski, S.D. Stranks, A. Abate, G. Sadoughi, A. Sadhanala, N. Kopidakis, G. Rumbles, C.-Z. Li, R.H. Friend, A.K.Y. Jen, H.J. Snaith, Heterojunction modification for highly efficient organic–inorganic perovskite solar cells, ACS Nano 8 (2014) 12701–12709.

[37] A. Al-Ashouri, E. Köhnen, B. Li, A. Magomedov, H. Hempel, P. Caprioglio, J. A. Márquez, A.B. Morales Vilches, E. Kasparavicius, J.A. Smith, N. Phung, D. Menzel, M. Grischek, L. Kegelmann, D. Skroblin, C. Gollwitzer, T. Malinauskas, M. Jost, G. Matic, B. Rech, R. Schlatmann, M. Topic, L. Korte, A. Abate, B. Stannowski, D. Neher, M. Stolterfoht, T. Unold, V. Getautis, A. Albrecht, Monolithic perovskite/silicon tandem solar cell with >29% efficiency by enhanced hole extraction, Science 370 (2020) 1300–1309.

[38] B. Niu, H. Liu, Y. Huang, E. Gu, M. Yan, Z. Shen, K. Yan, B. Yan, J. Yao, Y. Fang, H. Chen, C.-Z. Li, Multifunctional hybrid interfacial layers for high-performance inverted perovskite solar cells, Adv. Mater. 35 (2023) 2212258.

[39] X. Zhang, B. Li, S. Zhang, Z. Lin, M. Han, X. Liu, J. Chen, W. Du, G. Rahim, Y. Zhou, P. Shi, R. Wang, P. Wu, T. Alshahrani, W. Alqahtani, N. Alahmad, Q. Wang, B. Ding, S. Dai, M.K. Nazeeruddin, Y. Ding, A spiro-type self-assembled hole transporting monolayer for highly efficient and stable inverted perovskite solar cells and modules, Energy Environ. Sci. 18 (2025) 468–477.

[40] H. Zhang, S. Zhang, X. Ji, J. He, H. Guo, S. Wang, W. Wu, W.-H. Zhu, Y. Wu, Formamidinium lead iodide-based inverted perovskite solar cells with efficiency over 25% enabled by an amphiphilic molecular hole-transporter, Angew. Chem. Int. Ed. 63 (2024) e202401260.

[41] H. Zhou, W. Wang, Y. Duan, R. Sun, Y. Li, Z. Xie, D. Xu, M. Wu, Y. Wang, H. Li, Q. Fan, Y. Peng, Y. Yao, C. Liao, Q. Peng, S. Liu, Z. Liu, Glycol monomethyl ether-substituted carbazolyl hole-transporting material for stable inverted perovskite solar cells with efficiency of 25.52%, Angew. Chem. Int. Ed. 63 (2024) e202403068.

[42] A. Sun, C. Tian, R. Zhuang, C. Chen, Y. Zheng, X. Wu, C. Tang, Y. Liu, Z. Li, B. Ouyang, J. Du, Z. Li, J. Cai, J. Chen, X. Wu, Y. Hua, C.-C. Chen, High open-circuit voltage (1.197 V) in large-area (1 cm2) inverted perovskite solar cell via interface planarization and highly polar self-assembled monolayer, Adv. Energy Mater. 14 (2024) 2303941.

[43] S. Cho, P. Pandey, S. Yoon, J. Ryu, D.-G. Lee, Q. Shen, S. Hayase, H. Song, H. Choi, H. Ahn, C.-M. Oh, I.-W. Hwang, J.-S. Cho, D.-W. Kang, Anchoring self-assembled monolayer at perovskite/hole collector interface for wide bandgap Sn-based solar cells with a record efficiency over 12%, Surfaces and Interfaces 42 (2023) 103478.

[44] D. Song, S. Ramakrishnan, Y. Zhang, Q. Yu, Mixed self-assembled monolayers for high-photovoltage tin perovskite solar cells, ACS Energy Lett. 9 (2024) 1466–1472.

[45] B. Li, C. Zhang, D. Gao, X. Sun, S. Zhang, Z. Li, J. Gong, S. Li, Z. Zhu, Suppressing oxidation at perovskite–NiOx interface for efficient and stable tin perovskite solar cells, Adv. Mater. 36 (2024) 2309768.

[46] C.-H. Kuan, S.N. Afraj, Y.-L. Huang, A. Velusamy, C.-L. Liu, T.-Y. Su, X. Jiang, J.-M. Lin, M.-C. Chen, E.W.-G. Diau, Functionalized thienopyrazines on NiOx film as self-assembled monolayer for efficient tin-perovskite solar cells using a two-step method, Angew. Chem. Int. Ed. 136 (2024) e202407228.

[47] A. Abid, A. Velusamy, S.N. Afraj, W. Pervez, T.-Y. Su, S.-H. Hong, C.-L. Liu, M.-C. Chen, E.W.-G. Diau, Phenothiazine-based self-assembled monolayers for efficient tin perovskite solar cells with Co-cations, J. Mater. Chem. A 13 (2025) 9252–9264.

[48] S.N. Afraj, C.-H. Kuan, H.-L. Cheng, Y.-X. Wang, C.-L. Liu, Y.-S. Shih, J.-M. Lin, Y.-W. Tsai, M.-C. Chen, E.W.-G. Diau, Triphenylamine-based Y-shaped self-assembled monolayers for efficient tin perovskite solar cells, Small 21 (2025) 2408638.

[49] S.N. Afraj, C.-H. Kuan, J.-S. Lin, J.-S. Ni, A. Velusamy, M.-C. Chen, E.W.-G. Diau, Quinoxaline-based X-shaped sensitizers as self-assembled monolayer for tin perovskite solar cells, Adv. Funct. Mater. 33 (2023) 2213939.

[50] P.J. Hotchkiss, S.C. Jones, S.A. Paniagua, A. Sharma, B. Kippelen, N.R. Armstrong, S.R. Marder, The modification of indium tin oxide with phosphonic acids: mechanism of binding, tuning of surface properties, and potential for use in organic electronic applications, Acc. Chem. Res. 45 (2012) 337–346.

[51] A. Velusamy, S. Yau, C.-L. Liu, Y. Ezhumalai, P. Kumaresan, M.-C. Chen, Recent studies on small molecular and polymeric hole-transporting materials for high-performance perovskite solar cells, J. Chin. Chem. Soc. 70 (2023) 2046–2063.

[52] S.N. Afraj, A. Velusamy, C.-Y. Chen, J.-S. Ni, Y. Ezhumalai, C.-H. Pan, K.-Y. Chen, S.-L. Yau, C.-L. Liu, C.-H. Chiang, C.-G. Wu, M.-C. Chen, Dicyclopentadithienothiophene (DCDTT)-based organic semiconductor assisted grain boundary passivation for highly efficient and stable perovskite solar cells, J. Mater. Chem. A 10 (2022) 11254–11267.

[53] V. Joseph, A.A. Sutanto, C. Igci, O.A. Syzgantseva, V. Jankauskas, K. Rakstys, V.I. E. Queloz, H. Kanda, P.-Y. Huang, J.-S. Ni, S. Kinge, M.-C. Chen, M.K. Nazeeruddin, Stable perovskite solar cells using molecularly engineered functionalized oligothiophenes as low-cost hole-transporting materials, Small 17 (2021) 2100783.

[54] S. Yu, Z. Xiong, H. Zhou, Q. Zhang, Z. Wang, F. Ma, Z. Qu, Y. Zhao, X. Chu, X. Zhang, J. You, Homogenized NiOx nanoparticles for improved hole transport in inverted perovskite solar cells, Science 382 (2023) 1399–1404.

[55] Q. Cao, T. Wang, X. Pu, X. He, M. Xiao, H. Chen, L. Zhuang, Q. Wei, H.-L. Loi, P. Guo, B. Kang, G. Feng, J. Zhuang, G. Feng, X. Li, F. Yan, Co-self-assembled monolayers modified NiO for stable inverted perovskite solar cells, Adv. Mater. 36 (2024) 2311970.

[56] M.-F. Falzon, M.M. Wienk, R.A.J. Janssen, Designing acceptor polymers for organic photovoltaic devices, J. Phys. Chem. C 115 (7) (2011) 3178–3187.

[57] V.M. Le Corre, E.A. Duijnstee, O. El Tambouli, J.M. Ball, H.J. Snaith, J. Lim, L.J. A. Koster, Revealing charge carrier mobility and defect densities in metal halide perovskites via space-charge-limited current measurements, ACS Energy Lett. 6 (2021) 1087–1094.

[58] P.N. Murgatroyd, Theory of space-charge-limited current enhanced by Frenkel effect, J. Phys. D. Appl. Phys. 3 (1970) 151.